Spontaneous formation of magnetic-plasmonic liposomes with tunable optical and magnetic properties

Authors: Jacopo Cardellini[1]†, Alessandro Surpi[2], Beatrice Muzzi[3,4], Valentina Pacciani[1], Claudia Innocenti[3], Claudio Sangregorio[3,4], Valentin Alek Dediu[2], Costanza Montis[1*], and Debora Berti[1]

Affiliations:

[1]Department of Chemistry "Ugo Schiff" and CSGI, University of Florence, via della Lastruccia 3, 50019 Sesto Fiorentino, Florence, Italy;

[2]Istituto per lo Studio dei Materiali Nanostrutturati – C.N.R., 40129, Bologna, Italy;

[3]Department of Chemistry "Ugo Schiff", University of Florence, via della Lastruccia 3, 50019 Sesto Fiorentino, Florence, Italy

[4]Institute of Chemistry of Organometallic Compounds − C.N.R., 50019 Sesto Fiorentino (FI), Italy

*Corresponding author: Costanza.montis@unifi.it

†Present address: Department of Chemistry and Applied Biosciences, Institute for Chemical and Bioengineering, ETH Zurich, Zurich, 8093, Switzerland

Keywords: Magnetic-plasmonic NPs, superparamagnetic NPs, plasmonic NPs, NPs-liposome hybrids, Multifunctional nanomaterials

Abstract:

Magnetoplasmonic NPs have shown remarkable potential in hyperthermia, Magnetic Resonance Imaging (MRI), and Surface Enhanced Raman Scattering (SERS) imaging and diagnostics. However, despite their potential, effective clinical translation remains extremely limited due to a lack of fundamental knowledge about the biological response to these materials, and ongoing efforts seek to bridge the gap between nanomaterial production and effective application. To overcome these hurdles, the combination of inorganic NPs with lipid membranes has emerged as a promising strategy for the biocompatibilization of nanomaterials, preserving the inherent properties of each component and exhibiting novel synergistic functionalities. In this study, we synthesize magnetic-plasmonic-liposome adducts via spontaneous self-assembly. The interaction between magnetic-plasmonic NPs and liposomes was addressed from a physicochemical point of view as a function of liposome composition and concentration. By combining Cryogenic Microscopy, UV-visible spectroscopy and Dynamic Light Scattering we demonstrated that the rigidity of the lipid membrane affects the aggregation of the NPs and the colloidal stability of the NPs-vesicle hybrids. The magnetic

responsivity of the hybrids is enhanced as a consequence of the colocalization and crowding of NPs on the lipid membranes and can be finely modulated by varying the number of particles per vesicle. Overall, these results pave the way for the development of multifunctional materials with controlled magnetic-plasmonic properties for a variety of technological applications.

1. Introduction

Over the last decade, the application of nanoparticles (NPs) for biomedical application has benefitted from the impressive developments of synthetic bottom-up methods for producing nanostructured materials. The use of nanomaterials for healthcare technologies potentially offers enormous advantages with respect to traditional methods, both in diagnostic, in imaging and in therapy (including surgery, chemotherapy, and radiation therapy).[1–4] Materials at the nanoscale have unique optical and magnetic characteristics suitable for a range of specific applications, that can be tailored by varying their composition, shape, size, and surface functionalization.[5–7] In this context, magnetoplasmonic NPs, .e. particles combining magnetic and plasmonic properties, are considered one of the most interesting and advanced material for biomedical applications.[8–10] Thanks to their superparamagnetic properties, they respond to static and alternating magnetic fields, making them attractive for the development of vectors for precise delivery of drugs[11–13]; furthermore, they can be efficient contrast agents in magnetic resonance imaging (MRI)[14] as well as therapeutic probes in hyperthermic treatments of tumours[15–17]. The functionalization of MNPs with gold (AuMNPs) allows for decreasing the overall reactivity of particles, enhancing the biocompatibility of the material, simultaneously introducing the characteristic plasmonic properties of nanostructured gold.[18,19] Importantly, such complex NPs can act as multifunctional nanosystems in multimodal bioimaging[20], where gold and magnetic moieties act as well-distinguishable contrast agents with additional hyperthermic and/or photothermal functions.[21,22] An arising strategy for further improving the NPs medical potential involves their combination with lipid membranes to develop smart engineered nanomaterials that not only retain the inherent properties of each component (biocompatibility of lipid scaffolds and electric, optical, magnetic, and catalytic properties of inorganic NPs) but also feature novel functionalities.[23–25] Recently, the combination of hydrophobic magnetic NPs (MNPs) with both lamellar and non-lamellar lipid assemblies has proved to be a valuable strategy to induce phase transition in lipid bilayers and controlled drug release.[26–28] However, in general, building-up a complex self-

assembled inorganic-organic system requires multiple synthetic steps, to achieve a controlled architecture with tailored colloidal and functional properties.[29–31]

Recently, we demonstrated that hydrophilic citrate-capped gold nanoparticles (AuNPs) spontaneously associate with the zwitterionic membrane of liposomes, forming AuNPs decorated liposome hybrids according to a membrane-templated process occurring *via* simple self-assembly steps.[32–36] This peculiar aggregative phenomenon, comporting the spectral variations of the plasmonic properties of AuNPs,[23,37–39] has been exploited in various colorimetric assays for the determination of rigidity[40] and concentration of synthetic and natural vesicles[41] as well as for estimating the degree of lipid coverage in membrane-camouflaged inorganic NPs.[42]

Here, we prepare citrate-capped magnetoplasmonic nanoparticles (Au@Fe_3O_4NPs) and physicochemically investigate their interaction with synthetic liposomes, aiming at exploring the possibility to exploit simple self-assembly steps for the preparation of controlled nanoparticles-liposome adducts with tailored optical and magnetic properties. To this aim, we first investigated the spontaneous assembly of the Au@Fe_3O_4NPs with two prototypical liposomal formulations of DOPC (1,2-Dioleoyl-sn-glycero-3-phosphocholine) and DPPC (1-dipalmitoyl-sn-glycero-3-phosphocholine), characterized by very different membrane rigidities. UV-Vis spectroscopy and Cryogenic Electron Microscopy (Cryo-EM) were combined to determine the morphology and plasmonic properties of Au@Fe_3O_4NPs-lipid vesicles hybrids, while Dynamic Light Scattering (DLS) was employed to determine their colloidal properties. Finally, a specifically designed magnetic mobility study demonstrated that the magnetic responsiveness of the NPs-vesicle suprastructures is highly enhanced compared to one of the free dispersed particles and, importantly, can be modulated by varying the NPs/vesicle ratio.

Overall, this work provides fundamental information on the spontaneous formation of magnetoplasmonic-liposome adducts, demonstrating how the spatial confinement of the particles on the liposome's membranes can be exploited to tune their magnetic response to an external magnetic field. The understanding of the chemical-physical parameters that rule this phenomenon as well as the ability to control the spontaneous assembly of magnetoplasmonic clusters on lipid scaffolds paves the way for the development of smart

multifunctional nanomaterials with biomedical and technological purposes, obtained *via* simple self-assembly steps.

1. Materials and Methods

2.1 Materials

Tetrachloroauric (III) acid and trisodium citrate dihydrate were provided by Sigma-Aldrich (St. Louis, MO). 1,2-Dioleoyl-sn-glycero-3-phosphocholine (DOPC) and 1-dipalmitoyl-sn-glycero-3-phosphocholine (DPPC) were provided by Avanti Polar Lipids. Milli-Q-grade water was used in all preparations.

2.2 Synthesis of Au@Fe3O4NPs

Au@Fe_3O_4NPs were synthetized according to a reported protocol with slight modifications.[43] Briefly, to prepare Fe3O4NPs, 0.811 g of FeCl3 and 0.497 g of FeCl2 were dissolved in 20 mL of milliQ water under constant agitation. Then, 2.5 mL of NH_4OH (28% w/v%) were added and the solution kept under agitation for 10 minutes. 2.2 g of sodium citrate were then added, and the temperature raised to 90°C for 30 minutes. The black dispersion was then slowly cooled to room temperature, rinsed 3 times with ethanol and dried under vacuum overnight. 5 mg of the so-obtained Fe_3O4NPs were dissolved in 10 mL of milliQ water. 20 mL of 0.5 mM $HAuCl_4$ water solution was brought to the boiling temperature under magnetic stirring. The Fe_3O_4NPs dispersion was then added to the mixture. The solution was further boiled for 10 minutes until a purple colour occurred. The Au@Fe_3O_4NPs solution was then cooled to room temperature and used without further purification steps.

2.3 Synthesis of liposomes

A proper amount of DOPC or DPPC was dissolved in chloroform, to obtain a lipid film by evaporating the solvent under a nitrogen stream and overnight vacuum drying. The film was then swollen with warm (50 °C) Milli-Q water and dispersed by vigorous vortex mixing to obtain a final 4 mg/ml lipid concentration. The resultant multilamellar vesicles (MVL) in water were subjected to 10 freeze−thaw cycles and extruded 10 times through two stacked polycarbonate membranes with a 100 nm pore size at room temperature to obtain

unilamellar vesicles (ULV) with a narrow and reproducible size distribution. The filtration was performed with the Extruder (Lipex Biomembranes, Vancouver, Canada) through Nuclepore membranes.

2.4 Synthesis of AuMNPs-liposome hybrids

Liposome-Au@Fe3O4 hybrids were obtained by incubating 300 µL 0.136 µM Au@Fe3O4 dispersion with different volumes (5, 8, 10, 20, and 50 µL) of 30 nM DOPC and DPPC dispersions, obtaining the following final liposomes concentration: 0.5, 0.8, 1, 2, and 5 nM.

2.5 UV-Vis

UV−Vis spectra were recorded with a Cary 3500 UV−vis spectrophotometer.

2.6 DLS

DLS at $\theta = 90°$ and ζ-potential measurements were performed using a Brookhaven Instrument 90 Plus (Brookhaven, Holtsville, NY). Each measurement was the average of 10 repetitions of 1 min each on the same sample, and measurements were repeated 10 times. The autocorrelation functions (ACFs) were analysed through a cumulant fitting stopped at the second order for samples characterized by a single monodisperse population, allowing an estimate of the hydrodynamic diameter of particles and the polydispersity index. For polydisperse samples, the experimental ACFs were analysed through Laplace inversion, according to the CONTIN algorithm. ζ-potentials were obtained from the electrophoretic mobility u according to Helmholtz−Smoluchowski equation $\zeta = (\frac{\eta}{\varepsilon}) \times \mu$ (1) where η is the viscosity of the medium and ε is the dielectric permittivity of the dispersing medium. The ζ-potential values are reported as averages from 10 measurements.

2.7 HR-TEM

High-Resolution transmission electron microscopy (HR-TEM) images were acquired on a ThermoFischer Talos F200X operated at 200 kV, which is equipped with an extreme field emission gun (FEG) electron source and Super-X Energy Dispersive X-ray Spectroscopy (EDS) system for chemical analysis.

2.8 Cryo-TEM

Cryo-EM data were collected at the Florence Center for Electron Nanoscopy (FloCEN), University of Florence, on a Glacios (Thermo Fisher Scientific) instrument at 200 kV equipped with a Falcon III detector operated in the counting mode. 3 μL of each sample was applied on glow-discharged Quantifoil Cu 300 R2/2 grids . The samples were plunge-frozen in liquid ethane using an FEI Vitrobot Mark IV (Thermo Fisher Scientific) instrument. Excess liquid was removed by blotting for 1 s using filter paper under 100% humidity and 10 °C. Images were acquired using EPU software with a physical pixel size of 2.5 Å and a total electron dose of ~ 50 e−/Å2 per micrograph.

2.9 PXRD

Powder X-Ray diffraction (PXRD) data were recorded using a Bruker New D8 ADVANCE ECO diffractometer equipped with a Cu Kα (1.5406 Å) radiation source and operating in θ-θ Bragg-Brentano geometry at 40 kV and 40 mA. The measurements were carried out in the range 15-70°, with step size of 0.03° and collection time of 1 s.

2.10 Magnetic measurements

Magnetic measurements were carried out on dried MNP samples by a MPMS SQUID magnetometer by Quantum Design, Ltd., operating in the 1.9-400 K temperature range and magnetic field up to 5 T. The hysteresis loop was acquired at room temperature (300 K), cycling the magnetic field between 5 T and -5 T. The Zero Field Cooled (ZFC)/ Field Cooled (FC) magnetization curves were acquired with a probe field of 50

Oe, after cooling the sample with (FC) and without (ZFC) the applied field. The blocking temperature (T_B) was estimated as the temperature at which the ZFC curve reaches its maximum value.

3 Result and discussion

3.1 Particle characterization (DLS, UV-vis, TEM, Magnetic properties)

A dispersion of Au@Fe_3O_4NPs at a concentration of 0.137 μM was prepared following a well-established protocol with minor adaptations (see section 2.2).[43] Initially, citrate-stabilized iron oxide NPs (Fe_3O_4NPs), prepared via a commonly employed synthetic route,[44] were added to a boiling solution of $HAuCl_4$ (see Supplementary Information for a comprehensive characterization of Fe_3O_4 NPs). The presence of citrate anions on the surface of Fe_3O_4 NPs induce the reduction of Au^{3+} ions, leading to the formation of Au@Fe_3O_4NPs heterostructures. The XRD pattern of the Fe_3O_4 seeds, reported in the SI, exhibited characteristic peaks consistent with the cubic spinel structure of magnetite (space group $Fd\bar{3}m$). The Rietveld analysis of the pattern indicated an average crystallite size of 8(1) nm with lattice parameter a = 0.8373(2) nm. The magnetic properties of the Fe_3O_4 powder were evaluated through hysteresis loop measurements at 300 K, revealing a saturation magnetization (Ms) of 53 emu/g and susceptibility (χ) of 11.5 e-2 emu/g/Oe (Figure 1a). The absence of hysteresis in the magnetization loop (negligible coercivity and remanence), suggested that the Fe_3O_4NPs are in the superparamagnetic regime at room temperature (300 K). This is corroborated by the blocking temperature value ($T_B \approx$ 110 K) estimated from the ZFC/FC magnetization curves (inset Fig.1a). Notably, the observed superparamagnetic behaviour aligns with the size range of the seeds.

Confirmation of the formation of hybrid nanostructures was obtained with UV-visible spectroscopy measurements (Figure 1b). The spectrum for Au@Fe_3O_4NPs exhibited a broad plasmonic peak centered at 538 nm, consistent with the formation of gold nanostructures. HR-TEM images and STEM-EDS element mapping distribution (Figure 1c) provided insight into the Au@Fe_3O_4 NPs' morphology, showing 40 $\pm$ 5 nm Au moiety surrounded by Fe_3O_4 seeds with average size 8 $\pm$ 2 nm. The hydrodynamic size of the particles was determined through DLS measurements. Figure 1d shows the measured autocorrelation function (red circles), and the relative size distribution obtained via a Non-Negatively constrained Least Squares model (NNLS). The NNLS, employed for colloidal dispersions of polydispersed particles, clearly distinguished between two distinct sizes

(inset in Figure 1d). The smaller population peaked at about 10 nm, perfectly matched the size of Fe_3O_4 seeds used as precursors. Simultaneously, the larger population, peaked at about 50 nm, agreed with the hydrodynamic size of the Au@Fe_3O_4 NPs. Collectively, these experimental finding provide clear evidence of the coexistence of 50 nm Au@Fe_3O_4NPs and 10 nm Fe_3O_4 magnetic seeds that have maintained their individuality not interacting with Au.

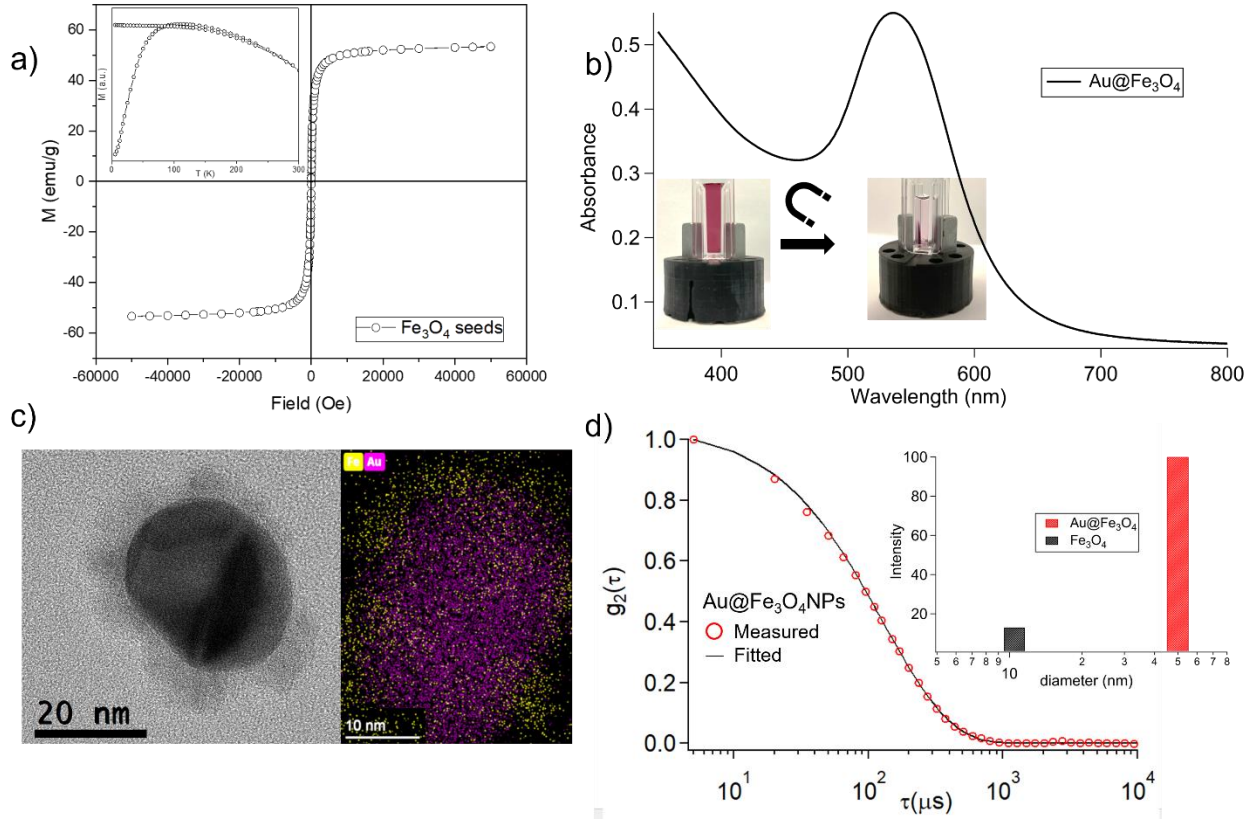

Figure 1: *a) Hysteresis loops of Fe_3O_4 NPs powder measured at 300 K. In the inset, the ZFC/FC magnetization curves are shown; b) UV-vis spectrum of 0.137 μM Au@Fe_3O_4NPs. The inset shows Au@Fe_3O_4NPs separated after 48h of contact with a magnet; c) HR-TEM image of the Au@Fe_3O_4 and STEM-EDS mapping for the chemical composition analysis; d) Autocorrelation function fitted by Laplace Inversion with NNLS algorithm. The inset shows the two particle populations obtained by the fitting.*

3.2 Structural analysis of Au@Fe3O4 -liposomes hybrids

To explore the interaction of the NPs with free-standing lipid membranes, Au@Fe_3O_4NPs were challenged with 100 nm monodispersed DOPC (1,2-Dioleoyl-sn-glycero-3-phosphocholine) and DPPC (1-dipalmitoyl-sn-glycero-3-phosphocholine) synthetic vesicles (see SI for the characterization). These chosen liposome

formulations differ significantly in terms of viscoelastic properties of the bilayers, which affect their response to external stimuli. Specifically, at room temperature, DOPC liposomes are characterized by a liquid-crystalline bilayer. Conversely, DPPC assembles in rigid membranes characterized by densely packed hydrophobic tails in the gel state.[45] In this study, owing to identical size, polydispersity, and hydrophilic heads' chemical nature, any observed difference in the interaction outcomes with Au@Fe_3O_4NPs can be attributed to the overall rigidity of liposomes, in turn determined by the bending modulus of the bilayer. Such stiffness has been shown as a pivotal factor in governing the interplay between lipid vesicles and citrate-coated gold nanoparticles.[32,40]

To unravel the structural aspects of the Au@Fe_3O_4NPs-liposome adducts, we performed cryo-EM microscopy. Figure 2 shows some representative images of Au@Fe_3O_4NPs with DOPC and DPPC vesicles after 10 minutes of incubation (additional Cryo-EM images are included in the SI). As shown, both Fe_3O_4 seeds and Au@Fe_3O_4NPs adhere to DOPC and DPPC vesicles without inducing observable membrane disruption. Yet, the rigidity of the bilayers distinctly shapes the morphology of the clusters. On soft DOPC vesicles, the NPs adhere to the lipid shell forming densely packed aggregates, characterized by direct particle-to-particle contact. Remarkably, the hybrids are characterized by a very high particle density per lipid vesicle. Conversely, on the more rigid DPPC lipid scaffolds, the clustering of NPs on the membrane surface is appreciably restrained. In the latter case, the average interparticle spacing of the Fe3O4 seeds and Au@Fe3O4 NPs adsorbed on the membranes is higher, and the number of adhered particles per vesicle is notably reduced. Interestingly, a similar effect was observed for liposomes interacting with citrate-coated AuNPs, despite the different nature of the NPs in terms of size and core composition.[32,36,39,42]

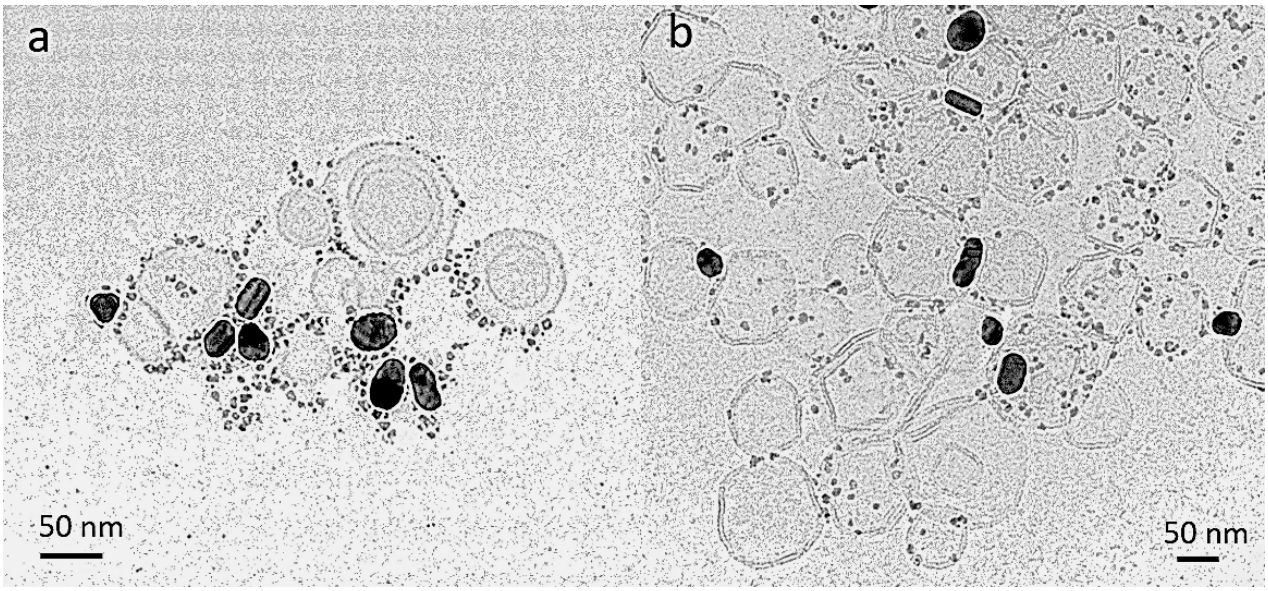

Figure 2: *Cryo-EM images of (a) DOPC-* Au@Fe_3O_4NPs *and (b) DPPC-* Au@Fe_3O_4NPs *composites.*

The crucial role of membrane rigidity on the interaction with Au@Fe_3O_4NPs is also apparent from the colour change of the dispersion, more pronounced and detectable, even to the naked eye, in the case of DOPC vesicles (see inset in Figures 3a and 3b). To quantitatively decipher the optical variations, we performed UV-Vis spectroscopy measurements. Figure 3 displays the UV-vis spectra collected the Au@Fe_3O_4NPs dispersions combined with varying concentrations of liposomes (0.5 nM, 0.8 nM, 1.0 nM, 2.0 nM, and 5.0 nM). Upon subjecting Au@Fe3O4NPs to DOPC liposomes, a red-shift and broadening of the original plasmonic peak of the particles occurs. In agreement with the insights gleaned from Cryo-EM images, this phenomenon stems from the coupling of Au@Fe_3O_4NPs plasmons, a consequence of their close spatial proximity, consistent with particle aggregation. Furthermore, a reduction in vesicle concentration corresponds to a progressive broadening of the plasmonic peak, pointing out that aggregation is maximized for lower DOPC amounts (Figure 1a). This experimental evidence suggests that, similarly to the observations with citrate-coated AuNPs, the membrane of soft vesicles induces the aggregation of the Au@Fe_3O_4NPs. Conversely, the interaction with rigid DPPC liposomes elicits a more modest bathochromic shift of the original peak, with minimal impact from vesicle concentration. These latter plasmonic changes correlate with a change in the chemical environment of the particles upon adhesion to the DPPC vesicles' surface. The inset of figure 3b, illustrates that the presence of the vesicles leaves the dispersion color unaltered, highlighting limited particle aggregation.

These results suggest that the phase of the membrane critically governs Au@Fe_3O_4NPs' aggregation, leading to the formation of completely different vesicle-NPs suprastructures, in line with the Cryo-EM images.

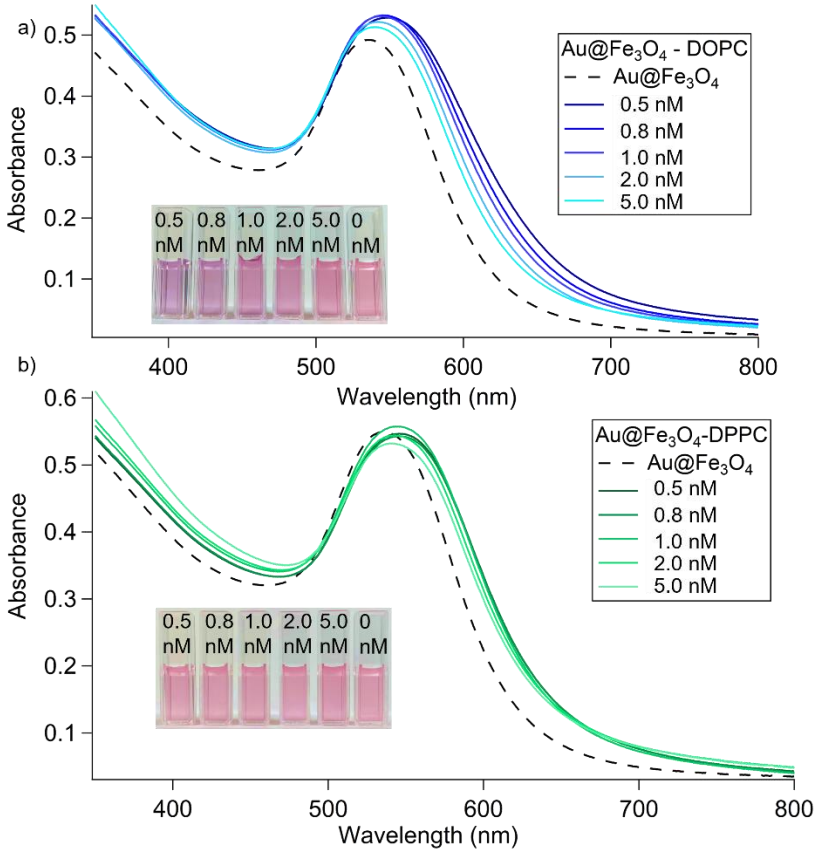

Figure 3: *UV-Vis absorption profiles of* Au@Fe_3O_4NPs *-DOPC (a) and* Au@Fe_3O_4NPs *-DPPC (b) as a function of the liposome concertation (0.5 nM, 0.8 nM, 1.0 nM, 2.0 nM, and 5.0 nM). The insets report the visual colour variation of the samples.*

3.3 Deciphering the Role of Fe_3O_4 Magnetic Seeds in Vesicle-NPs Interactions

DLS, HR-TEM, and Cryo-EM measurements demonstrated the coexistence of 10 nm Fe_3O_4 magnetic seeds and 50 nm Au@Fe_3O_4NPs. To understand whether the aggregation with liposomes originates from the Fe_3O_4 seeds or from the core-shell particles, we separated the two populations and tested their interaction with DOPC vesicles in separate experiments. The Au@Fe_3O_4NPs dispersion was centrifuged at 3000 rpm for 30 minutes (see Figure 4a). The resulting supernatant yielded a water dispersion of the Fe_3O_4NPs seeds and was employed as obtained. The red precipitate, exclusively containing Au@Fe_3O_4NPs particles, was subsequently re-dispersed in 1 mL of milliQ water.

Both dispersions underwent incubation with DOPC liposomes and were then analysed through DLS measurements. Regarding the interaction with the Au@Fe_3O_4NPs (Figure 4b, red circles), the analysis of the autocorrelation function unveiled the presence of two well-separated populations, centered at about 50 nm and 120 nm, matching the sizes of Au@Fe_3O_4NPs and DOPC liposomes, respectively. The identification of two distinct populations indicates the presence of non-interacting entities, characterized by their original diffusion coefficients. Conversely, incubation of the same liposomes with the supernatant (containing only 10-nm Fe_3O_4 seeds) leads to hybrids' formation with size matching the one obtained for the non-centrifugated Au@Fe_3O_4NPs (Figure 4b, green and purple circles).

Reasonably, this experimental evidence underscores that the absence of the small magnetic seeds inhibits the interaction between Au@Fe_3O_4NPs and the lipid membranes. Thus, aggregation between NPs and liposomes is triggered by the presence of 10 nm Fe_3O_4 seeds, ultimately involving Au@Fe_3O_4NPs, which then aggregate affecting the plasmonic properties of the dispersion.

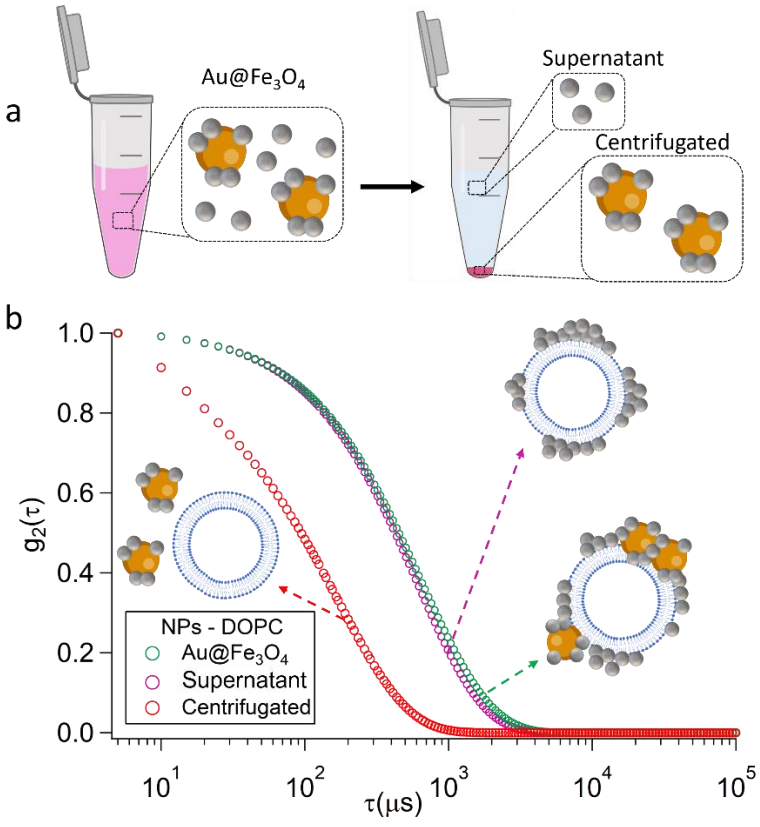

Figure 4: *a) Schematic illustration of Au@Fe_3O_4NPs dispersion before and after centrifugation; b) autocorrelation functions collected for* Au@Fe_3O_4NPs *-DOPC (green), Supernatant NPs-DOPC (purple), and*

centrifugated NPs-DOPC with respectively schematic representations of Au@Fe_3O_4NPs *-DOPC composites,* Fe_3O_4NPs *-DOPC composites and non-interacting DOPC with centrifugated* Au@Fe_3O_4NPs.

In recent experimental and theoretical investigations [32–34,39], focused on small (i.e., 12-15 nm diameter) citrate-capped AuNPs challenging soft lipid vesicles, the citrate capping agent emerged as the key player driving the interaction of AuNPs with the lipid membrane. The adhesion of AuNPs to soft lipid membranes initiates a ligand exchange between citrate, loosely bound to the Au surface, and the lipid polar heads [35,46,47]. The extent of ligand exchange depends on the contact area between the NP and the membrane, resulting from the balance between the AuNPs-DOPC adhesive forces and the bending modulus of the membranes, i.e. the energy cost required to deform the lipid bilayer from its spontaneous curvature[48]. The subsequent release of citrate triggers the clustering of electrostatically stabilized NPs, which spontaneously aggregate on the soft lipid membrane, where ligand exchange is maximized. Reasonably, in the present case, 10 nm citrate-capped Fe_3O_4NPs are able to elicit a similar effect, leading to particle aggregation, eventually encompassing larger Au@Fe_3O_4NPs. Conversely, as recently highlighted by Contini et al.,[49] when 50-60 nm NPs interact with liposomes, the adhesion to the membranes necessitates larger membrane modifications, leading to an increase in the membrane tension, which suppresses AuNPs clustering. In alignment with these findings, the adhesion of Au@Fe_3O_4NPs, in the absence of Fe_3O_4 seeds, is barely/not detectable. Overall, the simultaneous presence of small Fe_3O_4NPs seeds alongside larger Au@Fe_3O_4NPs emerges as pivotal to promote the formation of lipid vesicles-NPs suprastructures with magnetic and plasmonic properties.

3.4 Colloidal stability of AuMNPs-liposomes hybrids

We then investigated the colloidal stability of the lipid-NPs adducts, monitoring their hydrodynamic size over time via DLS. Figures 5a and 5b present the time evolution of the autocorrelation functions of the hybrids formed by interaction between Au@Fe_3O_4NPs and 1.0 mM DOPC and DPPC vesicles (additional DLS results are included in the SI). For DOPC, the interaction leads to kinetically stable hybrids with constant sizes over the first hour of incubation. In contrast, the Au@Fe_3O_4NPs adhesion on DPPC vesicles causes the fast formation of unstable micron-sized entities, which ultimately precipitate. As elucidated by the existing literature, the different in colloidal stability of inorganic NPs-liposome suprastructures is modulated by the

number of particles per vesicle.[50–54] A high number of adsorbed particles onto vesicle membranes imparts a charge to the hybrid, and stabilize the dispersion via electrostatic repulsion. As confirmed by Cryo-EM images, the soft DOPC bilayer triggers a massive docking of particles to the lipid shell. This relatively high number of NPs negatively charges the liposomal surface, providing electrostatic stabilization to the hybrids. In the case of DPPC, the membrane rigidity inhibits nanoparticle clustering, and the number of adsorbed NPs per vesicle is significantly lower. Reasonably, in this configuration, the particle number per vesicles fails to suffice electrostatic stabilization to the hybrids.

On the other side, the presence of adhered NPs introduces a nonuniform charge distribution which ultimately allows colloidal aggregation between hybrids. attractive forces towards surrounding vesicles, ultimately destabilizing the colloidal dispersion.

In summary, self-assembly and hybrid formation to magnetoplasmonic liposomal suprastructures is driven by the phase of the liposomal membrane, both in terms of morphology if the structures and in terms of their colloidal stability.[32]

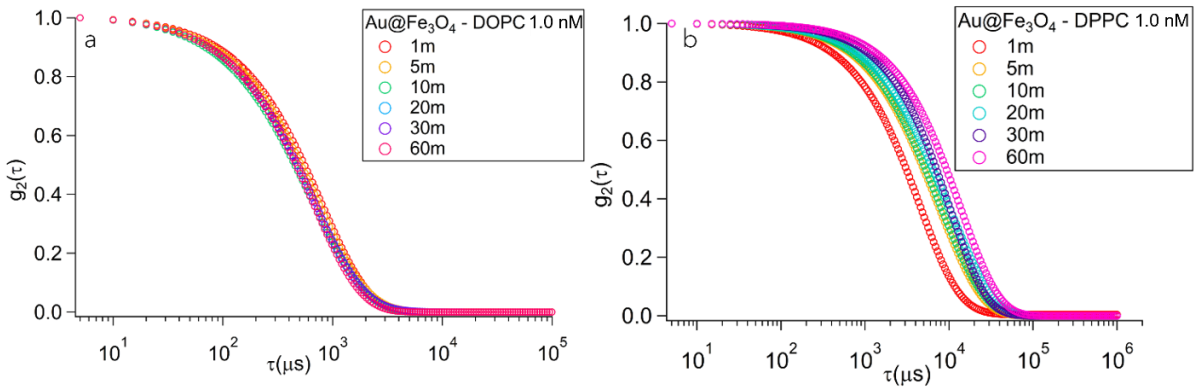

Figure 5: *Time evolution of the DLS curves of* Au@Fe_3O_4NPs-*DOPC hybrids (a) and* Au@Fe_3O_4NPs-*DPPC hybrids(b).*

3.5 Magnetic mobility of Au@Fe3O4NPs -DOPC hybrids

Finally, we investigated the magnetic responsivity of the hybrids to an external magnetic field. For this purpose, we limited our investigation to Au@Fe_3O_4NPs dispersion and the kinetically stable DOPC-Au@Fe_3O_4NPs, as dictated by the experimental design, based on diffusion studies.

A series of DOPC-Au@Fe_3O_4NPs hybrids were prepared, varying the concentration of liposomes, and the obtained dispersions characterized through DLS. Figure 6 reports the collected autocorrelation functions. As shown in the inset, the hydrodynamic diameter progression from 160 nm to 300 nm with decreasing liposome concentration is the direct consequence of the formation of NPs-vesicles hybrids characterized by a progressively larger number of particles per vesicle and is approximately consistent with the hydrodynamic dimension of a lipid vesicle surrounded by a crust of nanoparticles.

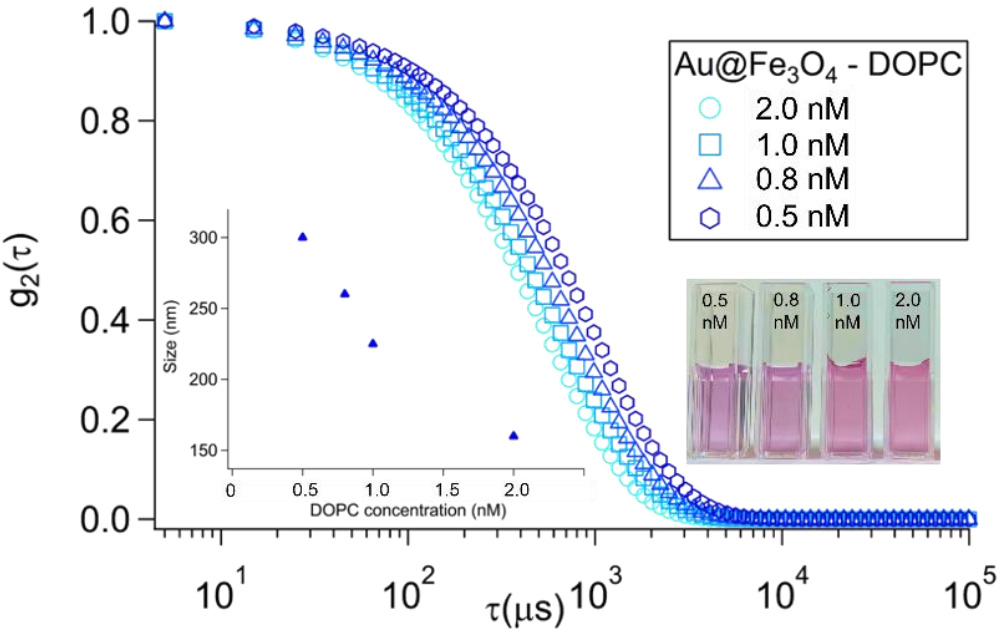

Figure 6: *Autocorrelation functions collected for Au@Fe_3O_4NPs-DOPC hybrids as a function of the liposome concentration (2.0 nM, 1.0 nM, 0.8 nM, and 0.5 nM).*

To better investigate the magnetic responsivity, a dedicated experimental set-up, developed at CNR-ISMN, was employed. In this setup, a dispersion of Au@Fe_3O_4NPs or Au@Fe_3O_4NPs-liposome hybrids was introduced into a 500 μm-wide quartz capillary, inserted into a high-gradient magnetic field generated by a couple of cubic permanent magnets placed on its sides. The asymmetric location of the capillary, offset approximately 200 μm from the system's central axis, enables the concentration of magnetic components of

the dispersion on one of its sides.[55] A microscope-connected CCD camera closely tracks the response of the Au@Fe3O4NPs-liposome hybrids (or Au@Fe3O4NPs) when exposed to a magnetic field. Within the dispersion, the magnetic field generates a drift of the magnetic objects towards the highest field regions, counteracted by Brownian motions. The competition between Brownian motion and directional magnetic forces defines the time scale for the evolution of the system, transitioning from a uniform dispersion to a non-uniform system, with accumulation of magnetic components in regions of intense magnetic influence.

Upon injection of the dispersions into the capillary, the particles will accumulate close to the magnet, forming a disc-shaped dark area, whose surface grows over time (see Figure 7a). A quantitative analysis of this phenomenon can be obtained measuring the product of the maximum number of CCD pixels occupied by the dark disc-shaped area in both the x- and y-directions. The evolution of this descriptor over time is reported for all the investigated samples (Figure 7b). This analysis clearly reveals distinct dynamics for Au@Fe_3O_4NPs and Au@Fe_3O_4NPs-liposome hybrids. The disc-shaped areas display a linear growth pattern for the hybrids, until a seemingly saturation condition in 1 and 3 hours for DOPC 0.5 nM and DOPC 0.8 nM samples, respectively. For the sample with the highest liposome/Au@Fe_3O_4NPs ratio (DOPC 2.0 nM), this plateau is not reached within the probed time range, and the surface area keeps growing linearly. For Au@Fe_3O_4NPs, the disc-shaped region initially grows exponentially, but transitions into a linear growth (i.e. constant growth rate) after, ca. 25000 seconds. In this case too, equilibrium is unattainable within the probed timeframe.

Upon closer scrutiny of the slopes from the linear fits (Table 1) of the disc areas over time, a consistent trend emerges. The growth rate increases with decreasing the liposome/Au@Fe_3O_4NPs ratio, indicating that increasing the magnetic particle number per vesicle amplifies the effects of the directional magnetic force over Brownian motion. In line with these results, for the dispersion Au@Fe_3O_4NPs, the time dynamics is the slowest of all the samples.

Sample	Growth rate ± statistical error	Pearson's r
Au@Fe_3O_4NPs/DOPC 0.5 nM	0.224 ± 0.020	0.96
Au@Fe_3O_4NPs /DOPC 0.8 nM	0.0671 ± 0.0027	0.991

Au@Fe_3O_4NPs /DOPC 2.0 nM	0.03523 ± 0.0013		0.98
Au@Fe_3O_4NPs	0.01645 ± 0.0023		0.81
	Exponential growth regime $y = Ae^{\frac{t}{\tau}}$		
	A	τ	Chi-Square
	1.1 ± 0.8	3690 ± 420	3120

Table 1: *Statistical values of the linear and exponential interpolations used to describe the accretion process.*

Overall, these results demonstrate that the membrane-templated aggregation of citrate-stabilized NPs can be instrumental in the production of novel ferrofluids based on magnetoplasmonic liposome suprastructures, having significantly distinct dynamics under an external magnetic field compared to the magnetic precursors. Furthermore, this temporal dynamic can be finely tuned through design, by changing the Au@Fe3O4NPs-liposome ratio, pointing out a promising pathway for applications in precision nanomedicine.

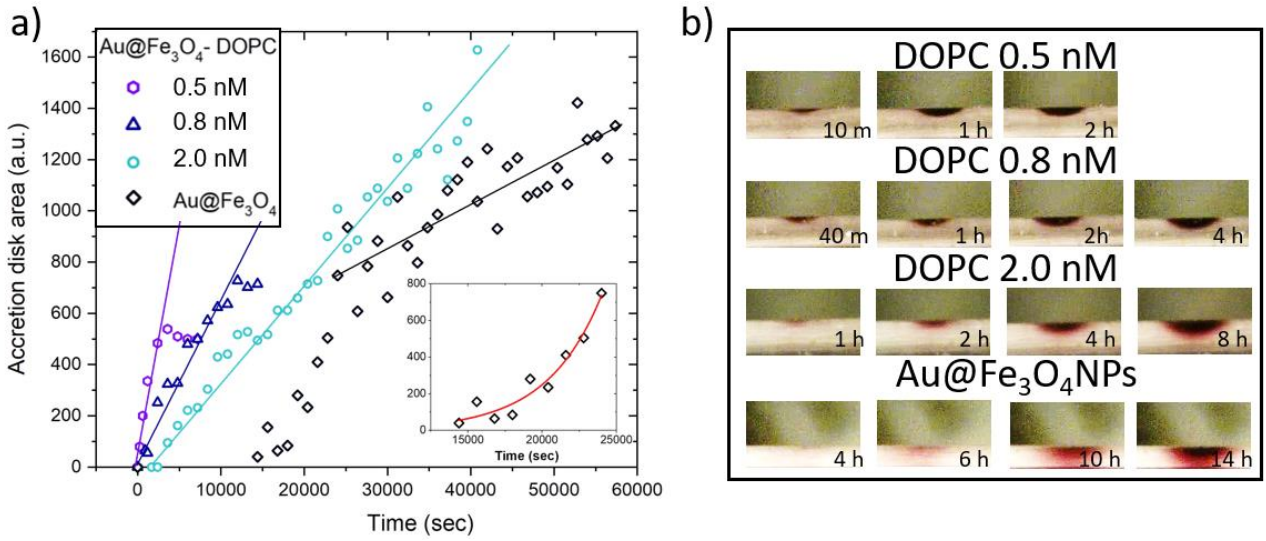

Figure 7: *a) Representative images of the accretion disks at different times for all the investigated samples. b) Time evolution of the area of the accretion disk for* Au@Fe_3O_4NPs *and* Au@Fe_3O_4NPs-*DOPC hybrids. Superimposed dashed lines represent the linear interpolations of experimental data. In the inset is shown the non-linear part of the time evolution for* Au@Fe_3O_4NPs *with the exponential interpolation superimposed.*

4 Conclusions

In conclusion, this study presented a comprehensive investigation into the self-assembly and format of hybrid magnetoplasmonic liposomal suprastructures composed of superparamagnetic Au@Fe_3O_4NPs and zwitterionic lipid vesicles. Through a combination of various techniques, including DLS, UV-Vis spectroscopy, TEM, Cryo-EM, and magnetic mobility studies, the interactions between the NPs and liposomes were elucidated. The findings have shed light on several key aspects: size, morphology, and colloidal stability of the resulting Au@Fe_3O_4NPs-liposome suprastructures can be finely controlled by varying the liposome compositions and relative Au@Fe_3O_4NPs/liposome ratio. Furthermore, a strong dependency on the rigidity of the lipid bilayer and of the membrane's phase emerged: while the incubation with stiff vesicles prevents the membrane-templated clustering of NPs, it also destabilizes the colloidal dispersion. Conversely the membrane of soft vesicles triggers the formation of compact NPs clusters on the liposomal surface, resulting in kinetically stable hybrids. Additionally, the number of NPs per vesicle and, thus, the hybrid size, can be tuned by varying the vesicle concentration. As demonstrated by magnetic mobility measurements, the magnetic responsivity of the hybrids is enhanced because of the accumulation of superparamagnetic particles on the lipid membranes. The observed dynamics under magnetic influence were influenced by the the number of particles per vesicle, highlighting the tunability of this behavior through design. The effects of membrane rigidity and NP-liposome ratios provide a promising path for tailoring the properties of these hybrids, potentially unlocking applications in fields ranging from nanomedicine to responsive materials, enabling simultaneous bioimaging, photothermal properties, magnetic hyperthermia, and targeted drug delivery. From a biomedical perspective, the combination of magnetic and plasmonic materials represents a tremendous opportunity, as it allows for the combination of all the characteristic properties of each specific component. By expanding our understanding of the interaction between nanoparticles and lipid membranes, this study contributes to increase the current knowledge of the phenomena occurring at the nano-bio interface but also to inform the design of lipid-NPs hybrids with tailored functionalities and responsive behaviors.

ACKNOWLEDGMENT

This work has been supported by the European Community through the BOW project (H2020-EIC-FETPROACT2019, ID 952183), by DoptoScreen project (Fondo di Beneficenza Intesa San Paolo 2019, B/2019/0289) and RISE project. The authors acknowledge MIUR-Italy (“Progetto Dipartimenti di Eccellenza 2018–2022, ref B96C1700020008” allocated to the Department of Chemistry “Ugo Schiff”) and the Center for Colloid and Surface Science (CSGI) for economic

support. We acknowledge the Florence Center for Electron Nanoscopy (FloCEN) at the University of Florence.

REFERENCES

1 M. Hofmann-Amtenbrink, D. W. Grainger and H. Hofmann, *Nanomedicine Nanotechnology, Biol. Med.*, 2015, **11**, 1689–1694.

2 M. S. Muthu, D. T. Leong, L. Mei and S. S. Feng, *Theranostics*, 2014, **4**, 660–677.

3 C. L. Ventola, D. J. Bharali and S. A. Mousa, *Pharmacol. Ther.*, 2010, **128**, 512–525.

4 C. L. Ventola, *P T*, 2017, **42**, 742–755.

5 L. Zhang, F. X. Gu, J. M. Chan, A. Z. Wang, R. S. Langer and O. C. Farokhzad, *Clin. Pharmacol. Ther.*, 2008, **83**, 761–769.

6 M. J. Mitchell, M. M. Billingsley, R. M. Haley, M. E. Wechsler, N. A. Peppas and R. Langer, *Nat. Rev. Drug Discov.*, 2021, **20**, 101–124.

7 M. Liong, J. Lu, M. Kovochich, T. Xia, S. G. Ruehm, A. E. Nel, F. Tamanoi and J. I. Zink, *ACS Nano*, 2008, **2**, 889–896.

8 Z. Ye, L. Lin, Z. Tan, Y.-J. Zeng, S. Ruan and J. Ye, *Appl. Surf. Sci.*, 2019, **487**, 1058–1067.

9 M. Ha, J.-H. Kim, M. You, Q. Li, C. Fan and J.-M. Nam, *Chem. Rev.*, 2019, **119**, 12208–12278.

10 B. Muzzi, M. Albino, A. Gabbani, A. Omelyanchik, E. Kozenkova, M. Petrecca, C. Innocenti, E. Balica, A. Lavacchi, F. Scavone, C. Anceschi, G. Petrucci, A. Ibarra, A. Laurenzana, F. Pineider, V. Rodionova and C. Sangregorio, *ACS Appl. Mater. Interfaces*, 2022, **14**, 29087–29098.

11 V. I. Shubayev, T. R. Pisanic and S. Jin, *Adv. Drug Deliv. Rev.*, 2009, **61**, 467–477.

12 D. D. Stueber, J. Villanova, I. Aponte, Z. Xiao and V. L. Colvin, *Pharmaceutics*, 2021, **13**, 943.

13 G. Mohammadi Ziarani, M. Malmir, N. Lashgari and A. Badiei, *RSC Adv.*, 2019, **9**, 25094–25106.

14 A. Avasthi, C. Caro, E. Pozo-Torres, M. P. Leal and M. L. García-Martín, 2020, pp. 49–91.

15 J. Jose, R. Kumar, S. Harilal, G. E. Mathew, D. G. T. Parambi, A. Prabhu, M. S. Uddin, L. Aleya, H. Kim and B. Mathew, *Environ. Sci. Pollut. Res.*, 2020, **27**, 19214–19225.

16 M. Bañobre-López, A. Teijeiro and J. Rivas, *Reports Pract. Oncol. Radiother.*, 2013, **18**, 397–400.

17 G. Pillai, *SOJ Pharm. Pharm. Sci.*, , DOI:10.15226/2374-6866/1/2/00109.

18 A. M. Alkilany, S. E. Lohse and C. J. Murphy, *Acc. Chem. Res.*, 2013, **46**, 650–661.

19 V. Amendola, R. Pilot, M. Frasconi, O. M. Maragò and M. A. Iatì, *J. Phys. Condens. Matter*, , DOI:10.1088/1361-648X/aa60f3.

20 C. de la Encarnación, E. Lenzi, M. Henriksen-Lacey, B. Molina, K. Jenkinson, A. Herrero, L. Colás, P. Ramos-Cabrer, J. Toro-Mendoza, I. Orue, J. Langer, S. Bals, D. Jimenez de Aberasturi and L. M. Liz-Marzán, *J. Phys. Chem. C*, 2022, **126**, 19519–19531.

21 C. de la Encarnación, D. Jimenez de Aberasturi and L. M. Liz-Marzán, *Adv. Drug Deliv. Rev.*, 2022, **189**, 114484.

22 C. Caro, F. Gámez, P. Quaresma, J. M. Páez-Muñoz, A. Domínguez, J. R. Pearson, M. Pernía Leal, A. M. Beltrán, Y. Fernandez-Afonso, J. M. De la Fuente, R. Franco, E. Pereira and M. L. García-Martín, *Pharmaceutics*, 2021, **13**, 416.

23 J. Liu, *Langmuir*, 2016, **32**, 4393–4404.

24 A. Luchini and G. Vitiello, *Front. Chem.*, 2019, **7**, 1–16.

25 M. Mendozza, L. Caselli, A. Salvatore, C. Montis and D. Berti, *Soft Matter*, 2019, **15**, 8951–8970.

26 A. Salvatore, C. Montis, D. Berti and P. Baglioni, *ACS Nano*, 2016, **10**, 7749–7760.

27 L. Caselli, M. Mendozza, B. Muzzi, A. Toti, C. Montis, T. Mello, L. Di Cesare Mannelli, C. Ghelardini, C. Sangregorio and D. Berti, *Int. J. Mol. Sci.*, , DOI:10.3390/ijms22179268.

28 C. Montis, B. Castroflorio, M. Mendozza, A. Salvatore, D. Berti and P. Baglioni, *J. Colloid Interface Sci.*, 2015, **449**, 317–326.

29 I. Rio, A. Rodrigues, J. Rodrigues, M.-J. Queiroz, R. Calhelha, I. Ferreira, B. Almeida, A. Pires, A. Pereira, J. Araújo, E. Castanheira and P. Coutinho, *Pharmaceutics*, 2021, **13**, 1905.

30 I. S. R. Rio, A. R. O. Rodrigues, C. P. Rodrigues, B. G. Almeida, A. Pires, A. M. Pereira, J. P. Araújo, E. M. S. Castanheira and P. J. G. Coutinho, *Materials (Basel).*, 2020, **13**, 815.

31 A. Tomitaka, H. Arami, Z. Huang, A. Raymond, E. Rodriguez, Y. Cai, M. Febo, Y. Takemura and M. Nair, *Nanoscale*, 2018, **10**, 184–194.

32 J. Cardellini, L. Caselli, E. Lavagna, S. Salassi, H. Amenitsch, M. Calamai, C. Montis, G. Rossi and D. Berti, *J. Phys. Chem. C*, 2022, **126**, 4483–4494.

33 S. Salassi, L. Caselli, J. Cardellini, E. Lavagna, C. Montis, D. Berti and G. Rossi, *J. Chem. Theory Comput.*, 2021, **17**, 6597–6609.

34 C. Montis, L. Caselli, F. Valle, A. Zendrini, F. Carlà, R. Schweins, M. Maccarini, P. Bergese and D. Berti, *J. Colloid Interface Sci.*, 2020, **573**, 204–214.

35 R. Kariuki, R. Penman, S. J. Bryant, R. Orrell-Trigg, N. Meftahi, R. J. Crawford, C. F. McConville, G. Bryant, K. Voïtchovsky, C. E. Conn, A. J. Christofferson and A. Elbourne, *ACS Nano*, 2022, **16**, 17179–17196.

36 A. Zendrini, J. Cardellini, R. Frigerio, M. Bertoni, D. Berti and P. Bergese, *JCIS Open*, 2023, **11**, 100088.

37 F. Wang and J. Liu, *Nanoscale*, 2015, **7**, 15599–15604.

38 F. Wang, D. E. Curry and J. Liu, *Langmuir*, 2015, **31**, 13271–13274.

39 J. Cardellini, C. Montis, F. Barbero, I. De Santis, L. Caselli and D. Berti, *Front. Bioeng. Biotechnol.*, , DOI:10.3389/fbioe.2022.848687.

40 L. Caselli, A. Ridolfi, J. Cardellini, L. Sharpnack, L. Paolini, M. Brucale, F. Valle, C. Montis, P. Bergese and D. Berti, *Nanoscale Horizons*, 2021, **6**, 543–550.

41 A. Zendrini, L. Paolini, S. Busatto, A. Radeghieri, M. Romano, M. H. M. Wauben, M. J. C. van Herwijnen, P. Nejsum, A. Borup, A. Ridolfi, C. Montis and P. Bergese, *Front. Bioeng. Biotechnol.*, 2020, **7**, 1–10.

42 J. Cardellini, A. Ridolfi, M. Donati, V. Giampietro, M. Severi, M. Brucale, F. Valle, P. Bergese, C. Montis, L. Caselli and D. Berti, *J. Colloid Interface Sci.*, 2023, **640**, 100–109.

43 H. Zhou, J. Lee, T. J. Park, S. J. Lee, J. Y. Park and J. Lee, *Sensors Actuators, B Chem.*, 2012, **163**, 224–232.

44 S. Laurent, D. Forge, M. Port, A. Roch, C. Robic, L. Vander Elst and R. N. Muller, *Chem. Rev.*, 2008, **108**, 2064–2110.

45 R. Michel and M. Gradzielski, *Int. J. Mol. Sci.*, 2012, **13**, 11610–11642.

46 H. Al-Johani, E. Abou-Hamad, A. Jedidi, C. M. Widdifield, J. Viger-Gravel, S. S. Sangaru, D. Gajan, D. H. Anjum, S. Ould-Chikh, M. N. Hedhili, A. Gurinov, M. J. Kelly, M. El Eter, L. Cavallo, L. Emsley and J. M. Basset, *Nat. Chem.*, 2017, **9**, 890–895.

47 G. S. Perera, S. A. Athukorale, F. Perez, C. U. Pittman and D. Zhang, *J. Colloid Interface Sci.*, 2018, **511**, 335–343.

48 J. F. Nagle, *Faraday Discuss.*, 2012, **161**, 11–29.

49 C. Contini, J. W. Hindley, T. J. Macdonald, J. D. Barritt, O. Ces and N. Quirke, *Commun. Chem.*, 2020, **3**, 130.

50 R. Michel, T. Plostica, L. Abezgauz, D. Danino and M. Gradzielski, *Soft Matter*, 2013, **9**, 4167–4177.

51 Y. Yu, S. M. Anthony, L. Zhang, S. C. Bae and S. Granick, *J. Phys. Chem. C*, 2007, **111**, 8233–8236.

52 V. J. Mohanraj, T. J. Barnes and C. A. Prestidge, *Int. J. Pharm.*, 2010, **392**, 285–293.

53 S. Thamphiwatana, V. Fu, J. Zhu, D. Lu, W. Gao and L. Zhang, *Langmuir*, 2013, **29**, 12228–12233.

54 L. Zhang and S. Granick, *Nano Lett.*, 2006, **6**, 694–698.

55 A. Surpi, T. Shelyakova, M. Murgia, J. Rivas, Y. Piñeiro, P. Greco, M. Fini and V. A. Dediu, *Sci. Rep.*, 2023, **13**, 5301.